University of Nebraska - Lincoln
DigitalCommons@University of Nebraska - Lincoln

Combustion Research at University of Nebraska-Lincoln | Mechanical & Materials Engineering, Department of

2-28-2006

Pope, D. and Gogos, G. "Numerical Simulation of Fuel Droplet Extinction Due to Forced Convection," Combustion and Flame, 142:89-106 (2005)

Follow this and additional works at: http://digitalcommons.unl.edu/mechengcombust

Part of the Heat Transfer, Combustion Commons

"Pope, D. and Gogos, G. "Numerical Simulation of Fuel Droplet Extinction Due to Forced Convection," Combustion and Flame, 142:89-106 (2005)" (2006). *Combustion Research at University of Nebraska-Lincoln*. Paper 3.
http://digitalcommons.unl.edu/mechengcombust/3

This Article is brought to you for free and open access by the Mechanical & Materials Engineering, Department of at DigitalCommons@University of Nebraska - Lincoln. It has been accepted for inclusion in Combustion Research at University of Nebraska-Lincoln by an authorized administrator of DigitalCommons@University of Nebraska - Lincoln.

Available online at www.sciencedirect.com
SCIENCE DIRECT®
Combustion and Flame 142 (2005) 89–106
Combustion and Flame
www.elsevier.com/locate/combustflame

Numerical simulation of fuel droplet extinction due to forced convection

Daniel N. Pope [1], George Gogos *

Department of Mechanical Engineering, University of Nebraska—Lincoln, Lincoln, NE, USA

Received 30 June 2004; received in revised form 15 January 2005; accepted 1 February 2005

Available online 2 April 2005

Abstract

The extinction of an envelope flame at the forward stagnation point of a liquid fuel droplet due to forced convection is numerically investigated. The droplet is oxidizing within an air stream at atmospheric pressure. Combustion is modeled using finite-rate chemical kinetics and a one-step overall reaction. The gas-phase solution is obtained using the quasi-steady equations of mass, momentum, species, and energy conservation. A new multicomponent formulation, which is appropriate for use with the finite-volume method, was developed to accurately describe the mass diffusion. Droplet circulation is accounted for by solving the quasi-steady mass and momentum conservation equations, for the liquid phase. The gas phase and liquid phase are coupled via interfacial conservation equations, and the complete set of governing equations is solved iteratively. Results for extinction velocity as a function of droplet diameter and freestream temperature are presented for an n-heptane droplet. Numerical predictions for n-heptane are in quantitative agreement with the limited n-heptane experimental data available in the literature, and in qualitative agreement with experimental results for a variety of fuels and over a wide range of ambient temperatures and droplet diameters. A linear dependence of the extinction velocity as a function of droplet diameter constitutes the present state of knowledge. This study predicts a nonlinear dependence for small diameters ($d < 1$ mm) and a linear dependence only for large diameters ($d > 2$ mm). The predictions also show that a form of the Damköhler number at extinction can be correlated with the Reynolds number through the use of the transfer number and appropriate dimensionless activation and adiabatic flame temperatures. A correlation that accurately reproduces the numerical predictions for extinction velocity over a wide range of droplet diameters and ambient temperatures is presented.
© 2005 The Combustion Institute. Published by Elsevier Inc. All rights reserved.

Keywords: Droplet combustion; Extinction; Finite volume; n-Heptane; Numerical simulation

* Corresponding author: Department of Mechanical Engineering, University of Nebraska—Lincoln, N104 Walter Scott Engineering Center, Lincoln, NE 68588-0656, USA. Fax: +1 402 472 1465.
E-mail address: ggogos@unl.edu (G. Gogos).

[1] Current address: Department of Mechanical and Industrial Engineering, University of Minnesota—Duluth, 105 VKH, 1305 Ordean Court, Duluth, MN 55812-3042, USA.

0010-2180/$ – see front matter © 2005 The Combustion Institute. Published by Elsevier Inc. All rights reserved.
doi:10.1016/j.combustflame.2005.02.010

Nomenclature

A	preexponential factor
a	fuel concentration exponent in reaction rate equation
B	transfer number
b	oxygen concentration exponent in reaction rate equation
c_p	specific heat capacity at constant pressure
$\bar{c}_{p,f}$	c_p of fuel at $\bar{T} = 0.5(T_{ad} + \bar{T}_s)$
d	droplet diameter
Da	Damköhler number
D_{ij}	binary diffusion coefficient for the pair ij
D_{im}	effective diffusion coefficient for the ith species
$D_{T,i}$	thermal diffusion coefficient for the ith species
E_a	activation energy
Gr	Grashof number
g	gravitational acceleration
h	specific enthalpy
K	evaporation constant
k	thermal conductivity
L	latent heat of vaporization
l	characteristic length
$\dot{m}''_\theta$	local mass flux at droplet surface
N	total number of chemical species
p	pressure
Q	lower heating value of fuel
R	droplet radius
Re	Reynolds number
Ri	Richardson number
R_f	ideal gas constant for fuel
R_u	universal gas constant
r	radial position
T	temperature
T_{ad}	adiabatic flame temperature
T_M	"mean" temperature $0.5(T_{ad} + T_\infty)$
$\bar{T}_s$	average droplet surface temperature
U_∞	freestream velocity
$\mathbf{V}_i$	diffusion velocity of the ith species
$\mathbf{v}$	velocity vector
v_r	velocity component in radial direction
v_θ	velocity component in polar direction
W_i	molecular weight of ith species
$\mathbf{W}_i$	component of $\mathbf{V}_i$ caused by temperature gradient
X_i	mole fraction of ith species
Y_i	mass fraction of ith species
y	flame distance from droplet surface along line of constant θ

Greek symbols

$\delta\mathbf{V}_i$	correction velocity for $\mathbf{V}_i$
ϵ	dimensionless activation temperature
μ	dynamic viscosity
ν	kinematic viscosity
ν''_i, ν'_i	stoichiometric coefficient of the ith product and reactant, respectively
ρ	density
σ	stoichiometric fuel-to-oxidizer (including inert species) mass ratio
θ	polar position
ω_i	rate of mass production of the ith species per unit volume

Subscripts

b	at boiling point
e	at extinction
f	fuel or flame
fc	forced convection
g	gas phase
i	ith species
l	liquid phase
M	properties evaluated at T_M and ambient composition
nc	natural convection
o	oxygen (O_2)
ox	oxidizer (dry air)
ref	reference state
s	droplet surface
sat	saturated liquid/vapor
∞	freestream or outer computational boundary

Superscripts

$*$	dimensionless variable
T	transpose

1. Introduction

The classic droplet combustion model (spherically symmetric envelope diffusion flame in a quiescent environment) predicts that any size droplet burns to completion [1]. However, the literature has shown that depending on the conditions, extinction is possible even in a quiescent environment. Thus, it has been known for a long time that small droplets could extinguish when the chemical reaction residence time is insufficient [2]. It has been shown both theoretically [3] and experimentally [4,5] that large droplets in a quiescent environment can extinguish when they experience excessive radiation heat losses from the flame zone. Furthermore, envelope flames surrounding droplets can extinguish in the presence of "adequately strong" convective flows.

Experimental studies on convective extinction of fuel droplets (mostly simulated with porous spheres) under normal gravity are also available in the literature [6–13]. The Richardson number (the inverse of the Froude number) provides a ratio of the strength of buoyancy-induced to forced convection flows in the experiments. It is given by

$$\mathrm{Ri} = \frac{\mathrm{Gr}}{\mathrm{Re}_{\infty,\mathrm{e}}^2} \approx \frac{g}{U_{\infty,\mathrm{e}}^2} \frac{l_{\mathrm{nc}}^3}{l_{\mathrm{fc}}^2},$$

where $U_{\infty,\mathrm{e}}$ is the characteristic velocity associated with forced convection at extinction conditions, l_{fc} is the characteristic length for forced convection, and l_{nc} is the characteristic length for natural convection. For $\mathrm{Ri} < O(10^{-1})$, forced convection dominates buoyancy [14]. The literature indicates that the extinction velocity increases monotonically with the droplet diameter (linearly [6] or like $d^{0.5}$ [8]). Regardless of the dependence, as a result of the monotonic increase in extinction velocity with droplet diameter, it has been argued that, under extinction conditions, natural convection becomes negligible (forced convection dominates and Ri is small) at large "droplet" (porous sphere) diameters (e.g., [12]). However, the effect of natural convection on extinction velocity depends on the orientation of the gravitational vector relative to the forced flow. In general, three different orientations have been used in experimental studies: the buoyancy-induced flow either (1) aids [7,9–12], (2) opposes [8], or (3) is normal to [6] the forced convection. The characteristic lengths in the Richardson number would differ greatly between these orientations. When the buoyancy-induced flow is normal to the forced convection, both l_{nc} and l_{fc} would be the lateral flame dimension (normal to the forced flow), which is approximately equal to the "droplet" diameter for the highly strained flames present in porous sphere extinction experiments. As a result, buoyancy is negligible in Spalding's experimental data [6] (Ri ranges from 0.14 to 0.045 for the range of diameters considered). If the buoyancy-induced flow aids or opposes the forced convection, l_{nc} becomes the total flame length (along the direction of the forced flow), whereas l_{fc} is approximately equal to the "droplet" diameter. The extinction flame length under these configurations can be many times larger than the "droplet" diameter (for large porous spheres it is on the order of 10 diameters [10]), which can lead to a nonnegligible buoyancy effect. The experiments of Agafonova et al. reported in Ref. [13] (air stream at room temperature) were conducted employing suspended droplets with the air stream aiding or opposing the buoyancy-induced flow. Extinction velocities of 0.4 and 0.8 m/s were measured, respectively, which shows convincingly the importance of natural convection.[2] Mixed convection is the prevailing flow field. No numerical study has attempted to simulate such an experiment.

In the absence of gravity, or when gravity and forced convection are collinear, an axisymmetric flow field surrounds a droplet. This makes the problem tractable for development of a numerical model. Studies using numerical models for droplet combustion under zero gravity and forced convection conditions are available in the literature [15–20]. No detailed numerical studies on the convective extinction of fuel droplets were found, with the exception of Jiang et al. [19], who predicted multiple flame configurations for a 100-μm-diameter droplet and specific combinations of Damköhler and Reynolds numbers.

A two-dimensional, axisymmetric model of droplet combustion must also contend with the computational requirements of modeling the combustion process. If the fuel is a typical hydrocarbon (e.g., n-heptane), then the detailed chemical kinetics may consist of hundreds of species and thousands of elementary reactions. The large number of species makes the use of detailed kinetics for long-chained hydrocarbons (in two-dimensional simulations) computationally prohibitive at present. Simplified or reduced chemical kinetics may be employed as an alternative to detailed kinetics. The simplest and most widely used mechanism is the one-step overall reaction [15–19]. The finite-rate chemical kinetics for the one-step overall reaction are empirical in nature and appropriate kinetic parameters could be determined from experimental data under microgravity conditions. Future work will undoubtedly use detailed kinetics to further delineate the effect of kinetics on fundamental

[2] When the air stream was at a high temperature, Agafonova et al. [13] reported that the extinction velocity was so large that buoyancy effects were negligible.

phenomena such as extinction. The numerical model of Lee et al. [20] can use detailed kinetics; however, results are presented for CO/air oxidation which consists of relatively few species.

Experimental studies on fuel droplet convective extinction under microgravity conditions are very limited. The microgravity studies currently available either give a range of possible extinction velocities (e.g., [21]) or merely note a specific flame configuration (e.g., wake [22] or envelope [4]) at a given freestream velocity. There are, however, several analytical/numerical studies available in the literature (including the closely related ones on flame extinction in the stagnation-point boundary layer [23–25]). All of these studies neglect gravity effects. Wu et al. [26] used the axisymmetric boundary layer equations with large activation energy asymptotics and predicted that the extinction velocity varies linearly with the droplet diameter, which is in agreement with the experiments of Spalding [6] and Sami and Ogasawara [9] and actually even with Agoston et al. [8], who curiously claimed a $d^{0.5}$ dependence although their data vary linearly with the diameter (see discussion on Fig. 3 below).

This article describes a numerical investigation of fuel droplet extinction due to forced convection. An environment consisting of air at atmospheric pressure is considered. The equations and methods employed in our numerical model are presented and numerical results are compared with experimental data available in the literature. Results for the extinction of n-heptane droplets in a zero-gravity environment at various temperatures are expressed as a function of droplet diameter. The Damköhler number at extinction is correlated with the Reynolds number through the use of the transfer number and appropriate dimensionless activation and adiabatic flame temperatures.

2. Theoretical model

A previously developed model for quasi-steady droplet combustion that used a single binary diffusion coefficient [27] has been modified to include the current multicomponent formulation and the effect of gravity. The model simulates the evaporation/combustion of a liquid fuel droplet of radius R in a convective, low-pressure environment of infinite expanse (Fig. 1). The freestream pressure (p_∞), temperature (T_∞), and velocity (U_∞) are constant. The model assumes a quasi-steady gas phase [28] with variable properties. Interaction between the gas and liquid at the interface causes circulation within the droplet and evaporation from the droplet surface. The liquid-phase quasi-steady equations with constant properties are incorporated to account for internal circulation and tangential velocities at the droplet surface. Other assumptions used to make the problem more tractable include: (1) the flow is axisymmetric and laminar; (2) the droplet maintains a spherical shape; (3) thermal radiation is negligible; (4) the Dufour effect and mass diffusion due to a pressure gradient, which are second-order effects, are negligible; (5) viscous dissipation and pressure work are negligible; (6) gas-phase transport and thermodynamic properties are a function of temperature and composition only; (7) the fuel droplet consists of a single component with negligible solubility of gas phase species into the liquid phase; and (8) heat transfer to the droplet interior is negligible. The gas phase consists of several different chemical species, the number and type of which are defined by the chosen fuel, the composition of the ambient gases, and the chemical kinetics model employed.

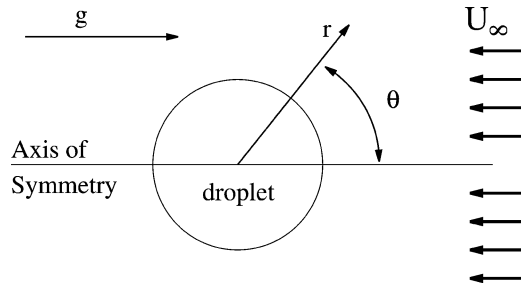

Fig. 1. Problem schematic (buoyancy-induced flow aiding forced convection).

The governing equations for the gas and liquid phases based on the above assumptions are shown below in vector form.

2.1. Gas phase

Continuity:

$$\nabla \cdot (\rho \mathbf{v}) = 0. \tag{1}$$

Conservation of species:

$$\nabla \cdot (\rho \mathbf{v} Y_i) = \omega_i - \nabla \cdot (\rho Y_i \mathbf{V}_i), \quad i = 1, \ldots, N. \tag{2}$$

Momentum conservation:

$$\rho \mathbf{v} \cdot \nabla \mathbf{v} = -\nabla p - \nabla \left[\frac{2}{3} \mu (\nabla \cdot \mathbf{v}) \right] + \nabla \cdot \left\{ \mu \left[(\nabla \mathbf{v}) + (\nabla \mathbf{v})^{\mathrm{T}} \right] \right\} + \rho \mathbf{g}. \tag{3}$$

Energy conservation:

$$\nabla \cdot (\rho \mathbf{v} T) = \nabla \cdot \left(\frac{k}{c_\mathrm{p}} \nabla T \right) + \frac{k}{c_\mathrm{p}^2} \nabla T \cdot \nabla c_\mathrm{p} - \frac{1}{c_\mathrm{p}} \sum_{i=1}^{N} \rho Y_i \mathbf{V}_i \cdot \nabla h_i - \frac{1}{c_\mathrm{p}} \sum_{i=1}^{N} \omega_i h_i. \tag{4}$$

Diffusion velocity:

$$\nabla X_i = \sum_{j=1}^{N}\left(\frac{X_i X_j}{D_{ij}}\right)(\mathbf{V}_j - \mathbf{V}_i) + \sum_{j=1}^{N}\left[\left(\frac{X_i X_j}{\rho D_{ij}}\right)\left(\frac{D_{\mathrm{T},j}}{Y_j} - \frac{D_{\mathrm{T},i}}{Y_i}\right)\right] \times \left(\frac{\nabla T}{T}\right), \quad i = 1, \ldots, N. \tag{5}$$

2.2. Liquid phase

Continuity:

$$\nabla \cdot \mathbf{v} = 0. \tag{6}$$

Momentum conservation:

$$\rho \mathbf{v} \cdot \nabla \mathbf{v} = -\nabla p + \mu \nabla^2 \mathbf{v} + \rho \mathbf{g}. \tag{7}$$

2.3. Interface conditions

The gas- and liquid-phase governing equations are coupled at the interface by the following equations, which are shown in spherical coordinates.

Continuity of tangential velocities:

$$v_{\theta,\mathrm{g,s}} = v_{\theta,\mathrm{l,s}}. \tag{8}$$

Continuity of shear stress:

$$\mu_{\mathrm{g,s}}\left[\frac{\partial v_{\theta,\mathrm{g}}}{\partial r} - \frac{v_{\theta,\mathrm{g}}}{r} + \frac{1}{r}\frac{\partial v_{r,\mathrm{g}}}{\partial \theta}\right]_{\mathrm{s}} = \mu_{\mathrm{l,s}}\left[\frac{\partial v_{\theta,\mathrm{l}}}{\partial r} - \frac{v_{\theta,\mathrm{l}}}{r} + \frac{1}{r}\frac{\partial v_{r,\mathrm{l}}}{\partial \theta}\right]_{\mathrm{s}}. \tag{9}$$

Conservation of species:

$$\text{fuel:} \quad \dot{m}''_\theta = \dot{m}''_\theta Y_{\mathrm{f,s}} + \rho_{\mathrm{g,s}} Y_{\mathrm{f,s}} V_{r,\mathrm{f,s}}, \tag{10}$$

$$\text{non-fuel:} \quad 0 = \dot{m}''_\theta Y_{i,\mathrm{s}} + \rho_{\mathrm{g,s}} Y_{i,\mathrm{s}} V_{r,i,\mathrm{s}}. \tag{11}$$

Conservation of energy:

$$\dot{m}''_\theta L = k_{\mathrm{g,s}} \left.\frac{\partial T_{\mathrm{g}}}{\partial r}\right|_{\mathrm{s}}. \tag{12}$$

Conservation of mass:

$$\dot{m}''_\theta = \rho_{\mathrm{g,s}} v_{r,\mathrm{g,s}} = \rho_{\mathrm{l,s}} v_{r,\mathrm{l,s}}. \tag{13}$$

Phase equilibrium is assumed at the droplet surface. The Clausius–Clapeyron equation was employed to relate the gas-phase surface temperature ($T_{\mathrm{g,s}}$) to the partial pressure of the fuel in the gas phase ($p_{\mathrm{g,f,s}}$):

$$\ln\left[\frac{p_{\mathrm{g,f,s}}}{p_{\mathrm{ref,sat}}}\right] = \frac{L}{R_{\mathrm{f}}}\left[\frac{1}{T_{\mathrm{ref,sat}}} - \frac{1}{T_{\mathrm{g,s}}}\right]. \tag{14}$$

2.4. Boundary conditions

The boundary conditions in terms of spherical coordinates are listed below.

Inflow: $r = r_\infty$, $0 \leqslant \theta \leqslant \pi/2$

$$v_r = -U_\infty \cos\theta,$$
$$v_\theta = U_\infty \sin\theta,$$
$$T = T_\infty,$$
$$p = p_\infty,$$
$$Y_i = Y_{i,\infty}, \quad i = 1, \ldots, N.$$

Outflow: $r = r_\infty$, $\pi/2 < \theta \leqslant \pi$

$$\frac{\partial v_\theta}{\partial r} = \frac{\partial T}{\partial r} = \frac{\partial p}{\partial r} = \frac{\partial Y_i}{\partial r} = 0.$$

The radial velocity (v_r) is extrapolated using the continuity equation.

Axis of symmetry: $\theta = 0$ or π

$$v_\theta = 0,$$
$$\frac{\partial v_r}{\partial \theta} = \frac{\partial T}{\partial \theta} = \frac{\partial p}{\partial \theta} = \frac{\partial Y_i}{\partial \theta} = 0$$

in both the gas and liquid phases.

2.5. Diffusion velocity

In anticipation of the use of the finite-volume method [29] to solve the governing equations, the diffusion velocity in the gas-phase conservation of species Eq. (2) must be described in terms of the gradient of the mass fraction of the ith species. Equation (5) states that mass diffusion consists of two components: "ordinary" diffusion, which is mass diffusion due to concentration gradients, and "thermal" diffusion (also known as the Soret effect), which is mass diffusion caused by temperature gradients. The diffusion velocities in Eq. (5) are linearly dependent and are subject to the constraint $\sum Y_i \mathbf{V}_i = 0$. The thermal diffusion coefficients have the following property: $\sum D_{\mathrm{T},i} = 0$ [30]. In the current model, the diffusion velocity is defined as

$$\mathbf{V}_i = -\frac{D_{i\mathrm{m}}}{Y_i}\nabla Y_i + \delta \mathbf{V}_i + \mathbf{W}_i,$$

where

$$\mathbf{W}_i = -\frac{D_{\mathrm{T},i}}{\rho Y_i}\frac{\nabla T}{T}$$

is the "thermal" diffusion velocity,

$$D_{i\mathrm{m}} = \frac{1 - X_i}{\sum_{j \neq i}(X_j / D_{ij})}$$

is the effective diffusion coefficient for the ith species into the mixture of all other species (see, e.g., [30] and Method V in [31]), and $\delta\mathbf{V}_i$ is a correction velocity to satisfy Eq. (5). Using the identities $\sum Y_i = 1$ and $X_i = (Y_i/W_i)/\sum(Y_j/W_j)$ (where W_i is the molecular weight of the ith species) in the above equations and rearranging give an expression for the correction velocities,

$$\delta\mathbf{V}_i \sum_{j\neq i} \frac{Y_j}{W_j D_{ij}} - \sum_{j\neq i} \frac{Y_j}{W_j D_{ij}} \delta\mathbf{V}_j = \sum_{j\neq i} \frac{1}{W_j}\left(1 - \frac{D_{j\mathrm{m}}}{D_{ij}}\right)\nabla Y_j, \tag{15}$$

for $i = 1, \ldots, N$ which are subject to the constraint

$$\delta\mathbf{V}_i + \sum_{j\neq i} Y_j \delta\mathbf{V}_j = \sum_{j=1}^{N} D_{j\mathrm{m}} \nabla Y_j + \delta\mathbf{V}_i(1 - Y_i). \tag{16}$$

The resulting gas-phase conservation of species equation, which is appropriate for use with the finite-volume method, is

$$\nabla \cdot \left[\rho(\mathbf{v} + \delta\mathbf{V}_i + \mathbf{W}_i)Y_i\right] = \omega_i + \nabla \cdot (\rho D_{i\mathrm{m}} \nabla Y_i).$$

2.6. Properties

Variable properties in the gas phase were calculated using the ideal gas law and low-pressure correlations from Reid et al. [32]. Species viscosities and thermal conductivities were calculated using the method of Chung et al. [32,33]. Mixture viscosity and thermal conductivity were obtained using the method of Wilke [32,34]. The curve fits of McBride et al. [35] were used to calculate the pure species-specific heat capacities and enthalpies with the corresponding values for the mixture given by

$$c_\mathrm{p} = \sum_{i=1}^{N} Y_i c_{\mathrm{p},i}$$

and

$$h = \sum_{i=1}^{N} Y_i h_i.$$

The binary diffusion coefficients D_{ij} were evaluated using the first approximation from kinetic theory [32, 36] and the Lennard–Jones 12–6 potential. Methods for calculating the thermal diffusion coefficient $D_{\mathrm{T},i}$ based on kinetic theory [36,37] are quite complex. An approximation developed by Ramshaw [38] was used to calculate $D_{\mathrm{T},i}$ in the gas phase.

The constant properties in the liquid phase were evaluated at the average surface temperature of the droplet. Values for the fuel density and viscosity were calculated using the correlations given by Haywood [39]. The latent heat of vaporization for the fuel was determined using the method of Pitzer et al. [32].

2.7. Combustion model

The fuel is n-heptane, which is oxidizing in dry air. A one-step overall reaction is used,

$$\mathrm{C_7H_{16}} + 11(\mathrm{O_2} + 3.77\mathrm{N_2}) \rightarrow 7\mathrm{CO_2} + 8\mathrm{H_2O} + 11(3.77\mathrm{N_2})$$

with the associated finite-rate chemical kinetics defined by

$$\omega_i = W_i(\nu_i'' - \nu_i')A\left(\frac{\rho Y_\mathrm{f}}{W_\mathrm{f}}\right)^a \left(\frac{\rho Y_\mathrm{o}}{W_\mathrm{o}}\right)^b \times \exp\left[\frac{-E_\mathrm{a}}{R_\mathrm{u}T}\right], \quad i = 1, \ldots, 5, \tag{17}$$

where ω_i is the rate of mass production of the ith species per unit volume, A is the preexponential factor, E_a is the activation energy, and a and b are the fuel and oxygen concentration exponents, respectively. Conversion of the governing equations to dimensionless variables (based on freestream values) yielded a dimensionless rate of species production (ω_i^*) of

$$\omega_i^* = \omega_i \frac{R}{U_\infty \rho_\infty}.$$

The resulting equation for ω_i^* is

$$\omega_i^* = \mathrm{Da}\,\frac{W_i}{W_\mathrm{f}}(\nu_i'' - \nu_i')(\rho^*)^{a+b} Y_\mathrm{f}^a Y_\mathrm{o}^b \times \exp\left[\frac{E_\mathrm{a}}{R_\mathrm{u}T_\infty} - \frac{E_\mathrm{a}}{R_\mathrm{u}T}\right],$$

where $\rho^* = \rho/\rho_\infty$ is the dimensionless density and

$$\mathrm{Da} = \frac{AR}{U_\infty}\rho_\infty^{a+b-1} W_\mathrm{f}^{1-a}\left(\frac{1}{W_\mathrm{o}}\right)^b \exp\left[\frac{-E_\mathrm{a}}{R_\mathrm{u}T_\infty}\right] \tag{18}$$

is the Damköhler number, which is the ratio of the convective time scale to the chemical reaction time scale.

The values for the kinetic parameters (A, E_a, a, and b) for a one-step overall reaction are determined empirically. Seiser et al. [40] suggest the following values for n-heptane: $A = 7.07 \times 10^{11}$ $(\mathrm{kmol/m^3})^{1-a-b}/\mathrm{s}$, $E_\mathrm{a} = 1.53 \times 10^5$ kJ/kmol, $a = 1.0$, and $b = 1.0$. They measured strain rate at extinction as a function of oxygen concentration for non-premixed flames stabilized in an oxidizer stream counterflowing over a liquid pool of n-heptane. The given kinetic parameters resulted in a match between their numerical predictions and experimental data. However, the experimental data were obtained under normal gravity and the numerical model neglected

gravity. Like Seiser et al. [40], the current work assumes that the reaction is first order with respect to fuel and oxygen ($a = b = 1$). However, appropriate values for A and E_a are determined by matching normal-gravity experimental data available in the literature with normal-gravity numerical results (see Section 4).

3. Numerical methods

The governing equations discussed in the previous section are discretized using the finite-volume [29] and SIMPLEC [41] methods. Convection/diffusion is modeled using the central difference with deferred correction method, with the "active" coefficients calculated using the power-law scheme [29]. A staggered grid was adopted to avoid zig-zag pressure distributions. Relaxation was incorporated via an artificial time step that was embedded in the discretization equations. Hyperbolic tangent stretching functions [42] were used to concentrate grid points near the fore and aft lines of symmetry and at the droplet surface in both the gas and liquid phases.

The discretization equations, with the exception of the diffusion velocity correction terms, were solved using the ADI method, with the TDMA used on each line of the two alternating directions. A single global iteration consisted of: (1) solution of the gas-phase discretization equations, (2) solution of the interface equations, (3) solution of the liquid-phase discretization equations, and (4) updating of the gas and liquid transport properties. The order of solution in the gas phase was: (1) solve the momentum equations, (2) solve the pressure correction equation, (3) correct the velocities and pressures, (4) solve for the diffusion velocity corrections, (5) solve the conservation of energy equation, (6) solve the first $N-1$ species conservation equations, and (7) solve for Y_N using $\sum Y_i = 1$. The solution procedure for the liquid phase was identical to steps (1) through (3) for the gas phase. Global convergence was defined as follows: For $\phi_{i,j} \geqslant \phi^{\max} \times 10^{-3}$,

$$\left| \frac{\phi_{i,j} - \phi_{i,j}^{\text{prev}}}{\phi_{i,j}} \right| \leqslant 1.0 \times 10^{-4}; \tag{19}$$

otherwise,

$$\left| \frac{\phi_{i,j} - \phi_{i,j}^{\text{prev}}}{\phi^{\max} \times 10^{-3}} \right| \leqslant 1.0 \times 10^{-4}, \tag{20}$$

where ϕ is $v_{r,\text{g}}$, $v_{\theta,\text{g}}$, T_g, $v_{r,\text{l}}$, or $v_{\theta,\text{l}}$; the superscript (prev) indicates the value at the previous global iteration; and $\phi^{\max}$ is the maximum velocity or temperature in the given phase. Equation (20) was included to allow for convergence when velocities near zero exist in the computational domain.

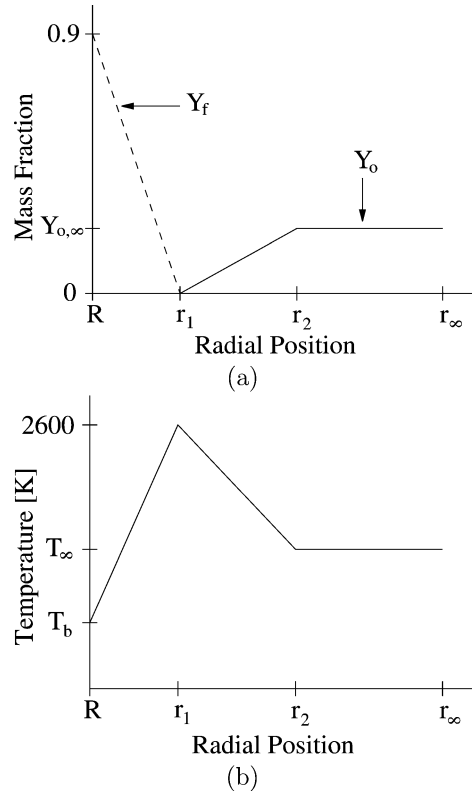

Fig. 2. Initial conditions for (a) fuel and oxygen mass fractions and (b) temperature distribution as a function of radial position.

The $N-1$ equations (15) along with the constraint equation (16), which define the diffusion velocity correction terms, were solved at each grid point using Gauss–Seidel iteration. Equation (16) was used for the correction term that corresponded to the species with the maximum Y_i.

Droplet ignition was accomplished numerically by assuming an initial condition of a chemically frozen environment with a high-temperature region surrounding the droplet. The velocities were initially set to zero in the computational domain. The fuel and oxygen mass fractions (Y_f and Y_o) were set as shown in Fig. 2a, with nitrogen (N_2) making up the balance of the total mass ($Y_{N_2} = 1 - Y_\text{o} - Y_\text{f}$). The assumed initial temperature distribution is shown in Fig. 2b. The values for r_1 and r_2 are adjustable program inputs which were varied until droplet ignition was achieved. When ignition occurs, results are independent of r_1 and r_2.

The extinction velocity was determined by selecting an initial freestream velocity that resulted in an envelope flame and then incrementing the freestream

velocity by 1 cm/s (0.5 cm/s for $d \leqslant 0.5$ mm) between successive quasi-steady solutions until a significant (greater than 5%) decrease in the evaporation constant (K) was obtained. This particular definition of extinction is consistent with experimental observations of the change in mass burning rate at extinction [8,10]. Physically, the extinction velocity corresponds to the maximum freestream velocity that will support an envelope flame. The evaporation constant (K) is an average over the entire droplet surface, and is given by

$$K = \frac{2}{\rho_l \pi R} \int_A \dot{m}''_\theta \, \mathrm{d}A.$$

The computer code developed for this study was extensively tested prior to its use for combustion simulations. Problems of increasing complexity were employed in the testing procedure which included the determination of minimum grid requirements. The details of the testing procedure and specific results are given in [27]. A brief summary of the testing procedure is provided below.

The gas-phase momentum, energy, and pressure correction equations were tested via comparison of the program output with numerical and experimental results for constant property flow over a sphere. The following data were used: (1) Drag coefficients for solid spheres at Reynolds numbers ($\mathrm{Re}_\infty = dU_\infty/\nu_\infty$) of 0.1, 1, 10, 100, and 300 were compared with numerical results in the literature [43–47] and with the correlations of Clift et al. [48]. (2) The dimensions of the attached vortex on the downstream side of the sphere were compared with the experimental results of Taneda [49] reported in [48]. (3) The angular location along the sphere surface at which the flow separates was compared with the correlation given by Clift et al. [48]. (4) Nusselt numbers for a Prandtl number of 0.672 and a dimensionless sphere temperature (T_s/T_∞) of 0.25 at Reynolds numbers of 0.1, 1, 10, and 50 were compared with the numerical results of Sayegh and Gauvin [46]. (5) Drag coefficients for blowing spheres at Reynolds numbers of 1 and 100 and blowing numbers ($\Lambda = v_{r,\mathrm{s}}/U_\infty$) of 0.1 and 0.3 were compared with the numerical results of Cliffe and Lever [50].

The liquid-phase momentum and pressure correction equations were tested by comparing results with the numerical predictions for isothermal flow past a water droplet of LeClair et al. [51]. Values for the location of the vortex in the liquid phase and the location and magnitude of the maximum velocity along the droplet surface were compared for Reynolds numbers of 30, 100, and 300.

The complexity of the problem under investigation makes an exhaustive study of the grid density requirements for all possible cases prohibitive. The above-mentioned test problems were used to generate a set of minimum grid requirements which were a function of Reynolds number. Sixty grid points in the polar direction ($n_\theta = 60$) and twenty-five grid points for the liquid-phase radial direction ($n_{r,\mathrm{l}} = 25$) are sufficient to maintain accuracy for Reynolds numbers up to 300. However, the number of radial grid points in the gas phase ($n_{r,\mathrm{g}}$), the dimensionless location of computational infinity ($r^*_\infty = r_\infty/R$), and the dimensionless grid spacing next to the droplet surface ($\Delta r^*_\mathrm{s} = \Delta r_\mathrm{s}/R$), are varied as a function of Reynolds number. For example, solutions with $100 < \mathrm{Re}_\infty \leqslant 300$ require $n_{r,\mathrm{g}} = 100$, $r^*_\infty = 15$, and $\Delta r^*_\mathrm{s} = 0.0125$, while solutions for $\mathrm{Re}_\infty = 0.001$ need $n_{r,\mathrm{g}} = 220$, $r^*_\infty = 150$, and $\Delta r^*_\mathrm{s} = 0.025$ to obtain solutions that are "grid independent" [27]. These grid requirements were used in initial runs for the combustion simulations that are discussed in Section 4. The actual $n_{r,\mathrm{g}}$ used for each of the runs was higher than the minimum values given to better resolve the flame locations. Also, several of the extinction runs that are presented exceed $\mathrm{Re}_\infty = 300$. Very dense grids in the polar direction ($n_\theta = 180$) and next to the droplet surface ($\Delta r^*_\mathrm{s} = 0.005$) were required for these cases.

The assembled code was also tested via comparison to the drag correlations of Chiang et al. [52] and Renksizbulut and Yuen [53], and to the Nusselt number correlations of Chiang et al. [52] and Renksizbulut and Yuen [54] for droplet evaporation. A Damköhler number of zero was specified in the code to obtain the results for droplet evaporation. Drag coefficients and Nusselt numbers for a 0.5-mm-diameter n-heptane droplet evaporating in air at temperatures of 800 and 1200 K were compared with the correlations over a range of Reynolds numbers from 5 to 100.

The results from the current code were in excellent agreement with all of the test cases listed in the preceding paragraphs. There were some slight differences in the evaporation data, with the two correlations bracketing results for drag coefficient from the current code and the current code predicting slightly lower Nusselt numbers (a maximum of 10% at $\mathrm{Re}_\infty = 5$) than both correlations (see Pope [27] for details). These slight differences are probably due to the use of different property correlations. Based on the level of agreement achieved with results in the literature for these "less complex" problems, the code was deemed sufficiently validated to explore its usefulness for combustion modeling.

4. Results

The experimental results of Gollahalli and Brzustowski [11] and Goldsmith [7] for the extinction velocities of n-heptane droplets under normal gravity

Table 1
Range of ambient temperatures and droplet diameters used in numerical results: n-heptane combustion in air at atmospheric pressure

T_∞ (K)	Diameters (mm)
300	0.1, 0.15, 0.2, 0.3, 0.5, 0.6, 0.8, 1, 1.3, 2, 3, 4.5, 6, 8, 15
650	0.1, 0.3, 0.5, 1, 2, 3, 4.5, 6, 8
673	0.1, 0.3, 0.5, 1, 2, 3, 4.5, 6, 8
800	0.1, 0.3, 0.5
1000	0.1, 0.3, 0.5, 1, 2, 3, 4.5, 6, 8
1140	0.1, 0.3, 0.5, 1, 2, 3, 4.5, 6, 8
1200	0.1, 0.3, 0.5, 1.3, 2
1400	0.1, 0.3, 0.5

were used to determine appropriate values for A and E_a in the combustion model. In both sets of experiments, the buoyancy-induced flow aided the forced convection flow (see Fig. 1). Gollahalli and Brzustowski [11] used a porous sphere of diameter $d = 6$ mm to determine the extinction velocity as a function of ambient pressure. Their experiments used n-heptane as the fuel and "room"-temperature air as the oxidizer. They report an extinction velocity of 0.5 m/s at a pressure of 1 atm. Goldsmith [7] used suspended fuel droplets with diameters between 1.5 and 1.8 mm in his experiments. He indicated that an envelope flame was not present at velocities above 0.345 m/s for an n-heptane droplet in air at "room" temperature and atmospheric pressure. Numerical simulations were conducted with $T_\infty = 300$ K, $p_\infty = 1$ atm, $g = 9.8$ m/s^2, and the buoyancy-induced flow aiding the forced convection. Use of the kinetic parameters $A = 3.35 \times 10^{11}$ m^3/(kmol s), $E_a = 1.53 \times 10^5$ kJ/kmol, $a = 1.0$, and $b = 1.0$ in the numerical model resulted in predicted extinction velocities of 0.35 and 0.5 m/s for $d = 1.65$ mm and $d = 6$ mm, respectively. The above kinetic parameters were used to generate the results given in the present work.

Numerical results are presented for the extinction velocities of n-heptane droplets burning in air at a pressure of 1 atm and under zero-gravity ($g = 0$) conditions. Droplet diameter (d) and freestream temperature (T_∞) are varied (Table 1) to determine their effect on extinction velocity ($U_{\infty,e}$). The available experimental data for extinction velocities under microgravity conditions have been used for model validation. In addition, experimental data for the extinction velocities of various fuels under normal gravity have been qualitatively compared with our zero-gravity numerical results for n-heptane.

First, the extinction velocity predicted by the current code is compared with the experimental value obtained by Okajima and Kumagai [21]. The close agreement between predicted and measured values instills confidence in the adopted kinetic parameters. For n-heptane and benzene droplets approximately 1.3 mm in diameter, Okajima and Kumagai [21] observed that an envelope flame could not be supported at velocities above 45 cm/s in their experiments. The experiments were conducted in air at atmospheric pressure and temperature. A drop tower was used to generate microgravity conditions. Air at atmospheric conditions was numerically modeled using $T_\infty = 300$ K and $p_\infty = 1$ atm. In the experiments, a spark was applied near the droplet to cause ignition. Droplet ignition was accomplished numerically through the use of the initial temperature and species mass fractions discussed previously. Based on these input conditions, the numerical model (without any adjustments) predicts an extinction velocity of 40 cm/s for $d = 1.3$ mm.

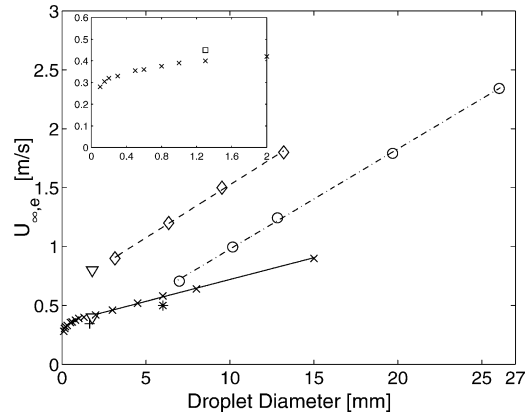

Fig. 3. Extinction velocity versus droplet diameter: (×) numerical predictions for n-heptane under zero gravity ($T_\infty = 300$ K, $p_\infty = 1$ atm). Experimental data for various fuels in air at "room" temperature and atmospheric pressure: under normal gravity: (○) kerosene (Spalding [6]), (◇) n-butyl alcohol (Agoston et al. [8]), (∗) n-heptane (Gollahalli and Brzustowski [11]), (▽) gasoline (Agafonova et al. [13], lower: aiding natural convection, upper: opposing natural convection), (+) n-heptane (Goldsmith [7]); under microgravity: (□) n-heptane (Okajima and Kumagai [21]).

Extinction velocities of droplets with diameters ranging from 0.1 to 15.0 mm were numerically determined for $T_\infty = 300$ K. The Reynolds number at extinction for the $d = 15.0$ mm case was $\mathrm{Re}_{\infty,e} = 863$. Numerical solutions for larger diameters (larger $\mathrm{Re}_{\infty,e}$) displayed instabilities (downstream temperature fluctuations did not allow for a converged solution) and are not included in the present work. Fig. 3 shows the predicted extinction velocity for n-heptane droplets in air as a function of droplet diameter. The figure also includes experimental results from the literature for the extinction velocity of various fuels under normal gravity.

Spalding [6] and Agoston et al. [8] conducted their experiments employing porous spheres. The experi-

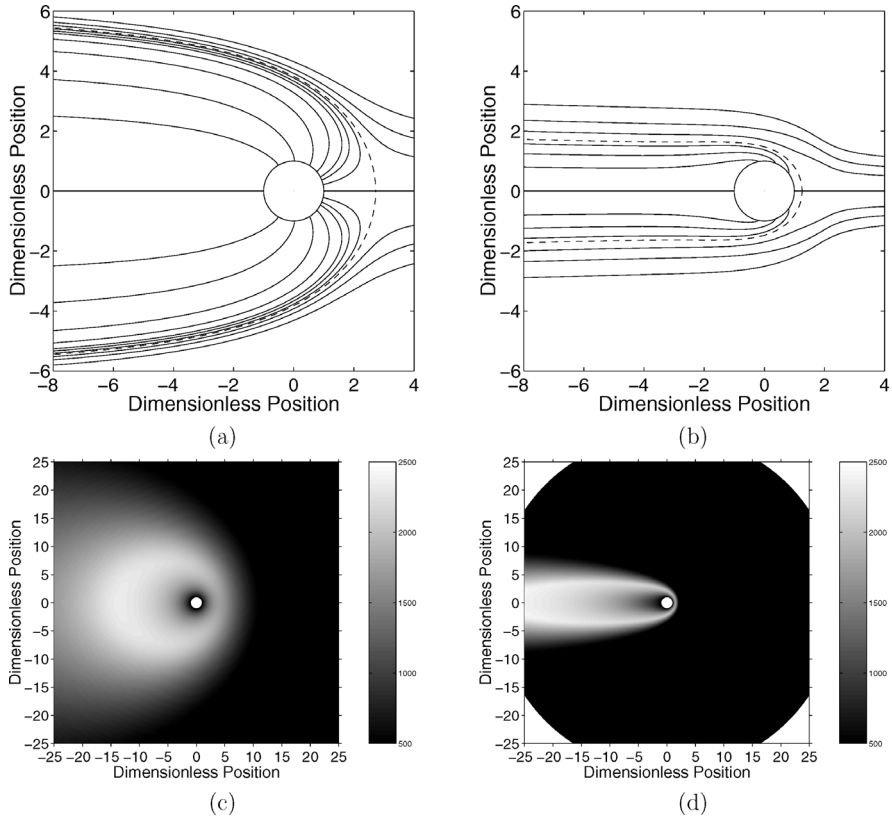

Fig. 4. Gas-phase streamlines (a, b) and grayscale plot of the temperature distribution in K (c, d) surrounding a typical small ($d = 0.2$ mm) and large ($d = 3$ mm) droplet at extinction; $T_\infty = 300$ K. $d = 0.2$ mm (a, c); $d = 3$ mm (b, d).

mental results of Spalding [6] for the extinction velocity of kerosene "droplets" under normal gravity and the nonturbulent data from Agoston et al. [8] for n-butyl alcohol under normal gravity are also shown in Fig. 3. Agoston et al. claimed that the extinction velocity was proportional to the square root of the droplet diameter; however, a linear variation of extinction velocity with respect to diameter appears to adequately describe their data over the range of diameters considered. Spalding's results also show that the extinction velocity varies linearly with diameter. The lines drawn through the data of Spalding (dash-dotted line) and Agoston et al. (dashed line) are least-squares curve fits of the data. Our numerical results (solid line) predict this linear dependence for approximately $d > 2$ mm. Large activation energy asymptotics [26] also predict this linear dependence. Obviously, the difference in magnitudes between our predictions and the measured extinction velocities in [6] and [8] is due to the difference in fuels. The experimental data of Gollahalli and Brzustowski [11] (asterisk) and Goldsmith [7] (plus sign), which were used to determine the kinetic parameters, are illustrated in Fig. 3. Both experiments employed the same fuel (n-heptane) as we did in our simulations. In both experiments, the buoyancy-induced flow aided the forced convection flow. Thus, the predicted extinction velocity under zero-gravity conditions is higher than the reported experimental values, as expected. Also shown in Fig. 3 are the extinction velocities measured by Agafonova et al. which are presented in Ref. [13]. They conducted the experiment so that the forced convection flow either aided or opposed the buoyancy-induced flow. They report extinction velocities of 0.4 and 0.8 m/s, respectively, for 1.8-mm-diameter suspended gasoline droplets. The effect of natural convection on extinction velocities is clearly demonstrated by these data.

In addition, Fig. 3 (inset) shows that for diameters in the range of 0.1–2.0 mm, our numerical model predicts that the extinction velocity exhibits a nonlinear dependence. Extrapolating the linear curve predicted for larger droplets may provide an erroneous value for extinction velocities of droplets of, say, 0.1 mm, which are encountered in a typical spray. The value of $U_{\infty,\mathrm{e}} = 0.45$ m/s for $d = 1.3$ mm (square) corresponds to the experimental results of Okajima and Kumagai [21], as previously discussed.

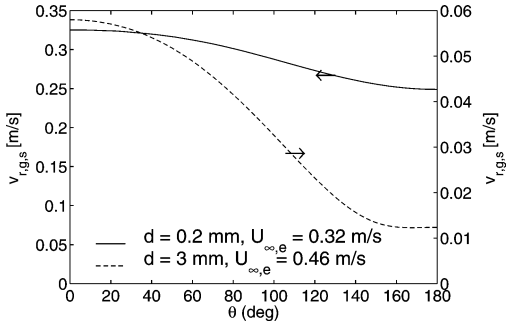

Fig. 5. Gas-phase radial velocity along the droplet surface for a typical small ($d = 0.2$ mm) and large ($d = 3$ mm) droplet at extinction; $T_\infty = 300$ K.

Fig. 4 illustrates the predicted flow and temperature fields around a typical small ($d = 0.2$ mm) and large ($d = 3$ mm) droplet at extinction for an ambient temperature of 300 K. Figs. 4a and 4b show the gas-phase streamlines surrounding the droplet for the $d = 0.2$ mm and $d = 3$ mm cases, respectively. The stagnation streamline is indicated by a dashed line. For $d = 3$ mm, extinction occurs at a Reynolds number of $\mathrm{Re}_{\infty,\mathrm{e}} = 88$, which indicates that forced convection is dominant for this case. As the droplet diameter decreases, the extinction velocity decreases, both quantities causing a reduction in the Reynolds number. For the $d = 0.2$ mm case, extinction occurs at a Reynolds number of $\mathrm{Re}_{\infty,\mathrm{e}} = 4.1$. At this low Reynolds number, the strength of the radial flow field due to droplet evaporation becomes comparable to the convective field strength.

Figs. 4c ($d = 0.2$ mm) and 4d ($d = 3$ mm) are grayscale plots of the temperature distribution surrounding the droplet. Both figures show trends similar to those of their corresponding streamline plots. The temperature distribution for the $d = 3$ mm case (Fig. 4d) shows a highly strained flame with a thin (compared to the droplet diameter) high-temperature zone near the forward stagnation point. In contrast, Fig. 4c ($d = 0.2$ mm) shows a very diffuse flame with a high-temperature region more than one diameter in thickness near the forward stagnation point.

Fig. 5 illustrates the predicted gas-phase radial velocity along the droplet surface ($v_{r,\mathrm{g,s}}$) for the same two cases shown in Fig. 4. The flame is closest to the droplet surface near the forward stagnation point, resulting in a higher local $v_{r,\mathrm{g,s}}$. The radial velocity along the droplet surface decreases by approximately 80% for the larger diameter ($d = 3$ mm). For the $d = 0.2$ mm case, the decrease in $v_{r,\mathrm{g,s}}$ is only 25%. The smaller diameter is approaching a constant $v_{r,\mathrm{g,s}}$ which is characteristic of spherically symmetric combustion. The extinction velocity ($U_{\infty,\mathrm{e}}$) is greater than $v_{r,\mathrm{g,s}}$ by an order of magnitude for the larger diameter ($d = 3$ mm). For the $d = 0.2$ mm case, $v_{r,\mathrm{g,s}}$ and $U_{\infty,\mathrm{e}}$ have approximately the same value. Despite the large difference in "blowing" velocities for the two cases, the presence of the envelope flame around the droplet results in a variation of less than 1 °C in the temperature along the droplet surface. The average droplet surface temperature for both cases, and for all of the cases given in Table 1, was approximately $\bar{T}_\mathrm{s} = 355$ K.

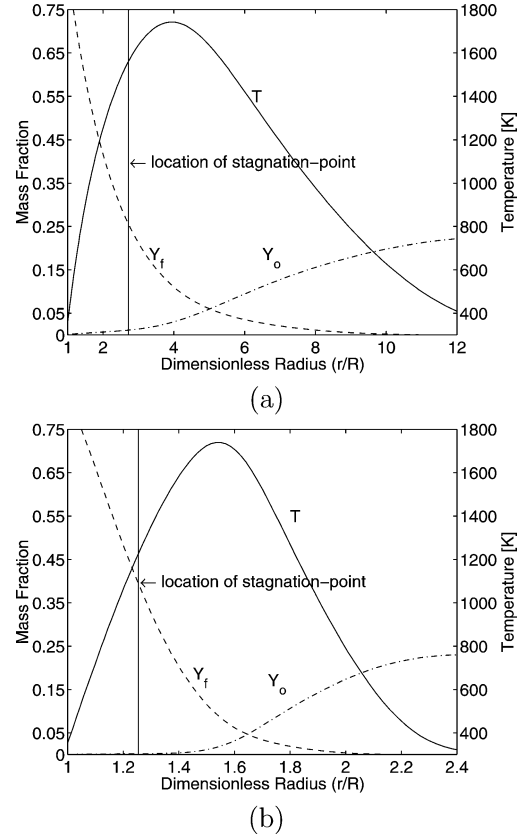

Fig. 6. Temperature distribution (in K) and fuel and oxygen mass fractions along the upstream axis of symmetry for a typical small ($d = 0.2$ mm) and large ($d = 3$ mm) droplet at extinction; $T_\infty = 300$ K. $d = 0.2$ mm (a); $d = 3$ mm (b).

Extinction of an envelope flame occurs somewhere near the forward stagnation point. Figs. 6a and 6b illustrate the temperature distribution and fuel and oxygen mass fractions along the upstream axis of symmetry ($\theta = 0$) for the same two cases shown in the previous two figures. The location of the stagnation point is also indicated on the figures. The "thin" (relative to the droplet diameter) reaction zone for the larger droplet (Fig. 6b) has been expanded to better display the temperature and mass fraction profiles. Both cases show a classic diffusion-flame profile, with fuel being supplied from the droplet surface and oxygen entering from the freestream. The location of maximum tem-

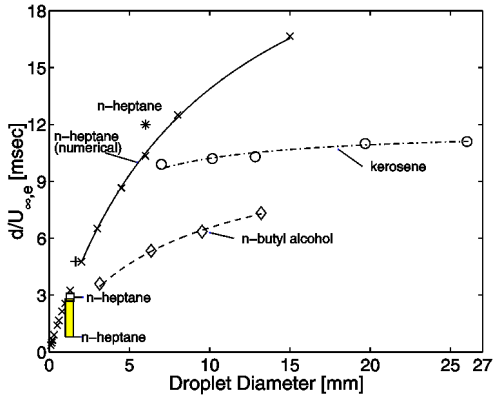

Fig. 7. Characteristic flow time at extinction versus droplet diameter: (×) numerical predictions for n-heptane under zero gravity ($T_\infty = 300$ K, $p_\infty = 1$ atm). Experimental data for various fuels in air at "room" temperature and atmospheric pressure: under normal gravity: (○) kerosene (Spalding [6]), (◇) n-butyl alcohol (Agoston et al. [8]), (∗) n-heptane (Gollahalli and Brzustowski [11]), (+) n-heptane (Goldsmith [7]), (shaded box) n-heptane (Chauveau et al. [55]); under microgravity: (□) n-heptane (Okajima and Kumagai [21]).

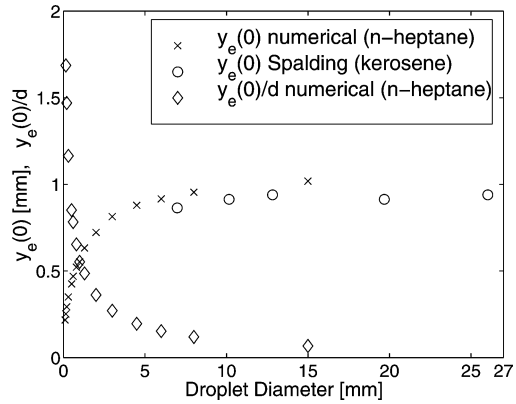

Fig. 8. Flame distance from the droplet surface along $\theta = 0$ at extinction versus droplet diameter: (×) $y_e(0)$ for n-heptane (numerical predictions), (○) $y_e(0)$ for kerosene (experimental, Spalding [6]), (◇) $y_e(0)/d$ for n-heptane (numerical predictions).

perature for the two cases is on the freestream side of the stagnation point. For conditions immediately prior to extinction, fuel and oxygen have started to "leak" through the flame front, with the leakage being more pronounced for the smaller droplet (low $\mathrm{Re}_{\infty,e}$). This leakage is not predicted for envelope flames that are farther away from extinction conditions. The results shown in Figs. 6a and 6b are typical of the results for all of the runs discussed in the present work.

Figs. 4, 5, and 6 show that, at extinction conditions, the flow and temperature distribution surrounding the droplet and the evaporation at the droplet surface differ significantly for droplet diameters in the linear ($d > 2$ mm) and nonlinear ($d < 1$ mm) regions noted in Fig. 3. The extinction Reynolds number increases with increasing droplet diameter. Its range in the nonlinear region is $O(1) \leqslant \mathrm{Re}_{\infty,e} \leqslant O(10)$. Forced convection dominates in the linear region, with the relative importance of diffusion increasing as droplet diameter is decreased. The flow field transition from a convection-dominated to an evaporation-dominated region manifests itself as a nonlinear dependence of the extinction velocity with the droplet diameter. This change in behavior at lower Reynolds numbers is implied in the asymptotic results of Wu et al. [26], who showed that the functional form of the droplet diameter at extinction changes when comparing extinction under forced convection at large Reynolds numbers (where boundary layer theory is applicable) and spherically symmetric conditions.

The characteristic flow time at extinction ($d/U_{\infty,e}$) as a function of droplet diameter is shown in Fig. 7. Spalding [6] observed a nearly constant flow time in his experiments using kerosene. This is to be expected, as extinction velocity varies linearly with diameter and intercepts the vertical axis at a small velocity, and only extinction velocities for large diameters are reported. The numerically predicted flow time for n-heptane increases with diameter at a decreasing rate and may approach a constant at much larger diameters. Additional experimental data for n-heptane, which have been obtained by Chauveau et al. [55] for suspended droplets under normal-gravity conditions and diameters between 1.0 and 1.5 mm, are shown in Fig. 7 (shaded box).

Fig. 8 presents information on $y_e(0)$, the flame distance from the droplet surface along $\theta = 0$ at extinction, as a function of droplet diameter. The flame distance is defined numerically as the location of maximum temperature. Spalding [6] noted that $y_e(0)$ was approximately constant (0.9 mm) in his experiments. Agoston et al. [8] reported the same result for a different fuel (n-butyl alcohol). Fig. 8 illustrates Spalding's data for kerosene and our numerical results for n-heptane. The numerical results are in good agreement with Spalding's data. For small diameters, a sharp decrease in the flame standoff distance is predicted. The ratio $y_e(0)/d$ is also shown in Fig. 8. For large diameters, $y_e(0)/d \ll 1$. Therefore, the "droplet" diameter is the characteristic length for natural convection when the buoyancy-induced flow is normal to the convective field. However, even though $y_e(0)$ decreases with droplet diameter, the ratio $y_e(0)/d$ increases to values greater than one for small droplets. Extinction occurs at "small" Reynolds numbers and the relative importance of diffusion (compared with forced convection) increases. The flame surrounding these small

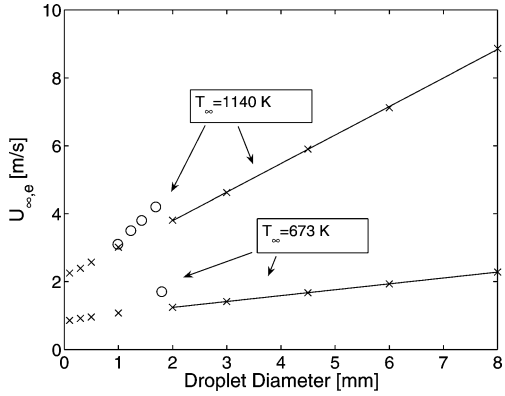

Fig. 9. Extinction velocity versus droplet diameter for $T_\infty = 673$ K and 1140 K ($p_\infty = 1$ atm): (×) numerical predictions for n-heptane under zero gravity, (○) experimental data for gasoline (Agafonova et al. [13]) under normal gravity.

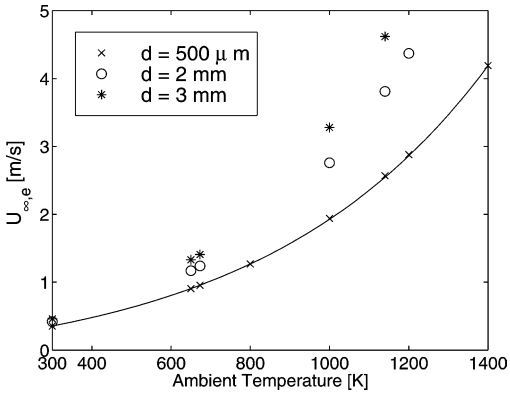

Fig. 10. Extinction velocity versus ambient temperature for different droplet diameters.

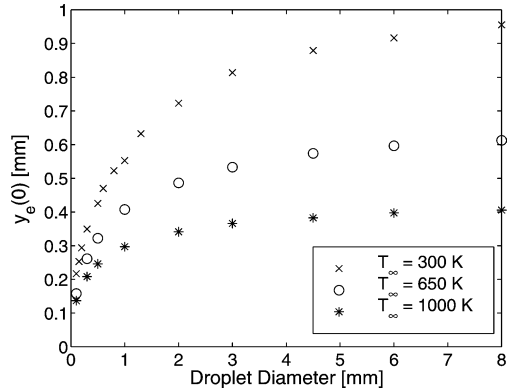

Fig. 11. Flame distance from the droplet surface along $\theta = 0$ at extinction versus droplet diameter for various ambient temperatures.

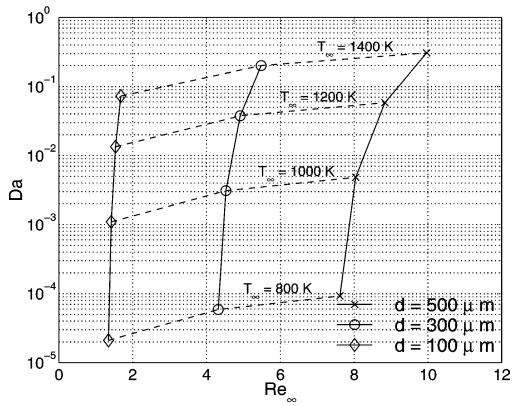

Fig. 12. Damköhler number versus Reynolds number at extinction for various droplet diameters and ambient temperatures.

droplets becomes closer to a spherically symmetric flame, resulting in a higher $y_e(0)/d$.

Solutions for the extinction of droplets with diameters ranging from 0.1 to 8.0 mm were obtained for $T_\infty = 673$ and 1140 K, and are shown in Fig. 9. Data from Agafonova et al. [13] for gasoline are included in the figure for qualitative comparison. The predicted linear region for extinction velocity as a function of diameter appears to extend to smaller diameters when the ambient temperature is elevated. As expected, much higher extinction velocities are predicted at these elevated ambient temperatures. This is shown clearly in Fig. 10, which contains the extinction velocity versus the ambient temperature for three different droplet diameters. The curve drawn through the results corresponding to $d = 500$ μm shows an exponential dependence of extinction velocity on ambient temperature. The increase in ambient temperature causes a decrease in the characteristic reaction time (through the exponential term in the Damköhler number, Eq. (18)), and therefore, a shorter convective time scale (higher velocity) is required for extinction. As a result of the higher velocity, the stagnation point and flame front move closer to the droplet surface, as shown in Fig. 11.

Extinction conditions are generally characterized in terms of the Damköhler number at extinction ($\mathrm{Da_e}$). Fig. 12 is a plot of the predicted Damköhler number versus Reynolds number at extinction for a range of droplet diameters ($d = 100, 300$, and 500 μm) and ambient temperatures ($T_\infty = 800, 1000$, 1200, and 1400 K). For a fixed diameter (solid lines), an envelope flame exists for conditions to the left of the curve. For a fixed ambient temperature (dashed lines), an envelope flame exists above the curve. The results shown in Fig. 12 indicate that a separate $\mathrm{Da_e}$-versus-$\mathrm{Re}_{\infty,e}$ curve exists for each specified d or T_∞. Jiang et al. [19] performed simulations only for $d = 100$ μm and, as a result, presented a single

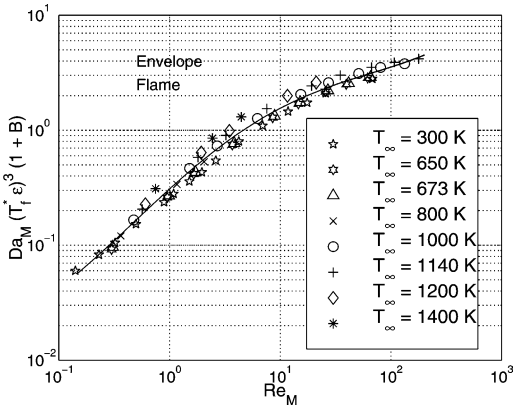

Fig. 13. Correlation of "scaled" Damköhler number versus Reynolds number at extinction for various droplet diameters and ambient temperatures.

curve. The following discussion presents an analysis that collapses all of the extinction conditions shown in Fig. 12 to a single curve.

The asymptotic results of Krishnamurthy et al. [25] for diffusion-flame extinction in a stagnation-point boundary layer suggest that the Damköhler number should scale with the adiabatic flame temperature, the activation temperature, and the transfer number. Fig. 13 is a plot of $\mathrm{Da}_{\mathrm{M,e}}(T_{\mathrm{f}}^{*}\epsilon)^{3}(1+B)$ versus $\mathrm{Re}_{\mathrm{M,e}}$ for all of the cases listed in Table 1. The Damköhler and Reynolds numbers at extinction are defined as

$$\mathrm{Da}_{\mathrm{M,e}} = \frac{AR}{U_{\infty,\mathrm{e}}}\rho_{\mathrm{M}}\frac{1}{W_{\mathrm{o}}}\exp\left[\frac{-E_{\mathrm{a}}}{R_{\mathrm{u}}T_{\mathrm{ad}}}\right] \tag{21}$$

and

$$\mathrm{Re}_{\mathrm{M,e}} = \frac{dU_{\infty,\mathrm{e}}}{\nu_{\mathrm{M}}},$$

where T_{ad} is the adiabatic flame temperature and the subscript "M" indicates that the properties are evaluated using the ambient composition (dry air) and a mean temperature of $T_{\mathrm{M}} = 0.5(T_{\mathrm{ad}} + T_{\infty})$. The dimensionless flame temperature (T_{f}^{*}), activation temperature (ϵ), and transfer number (B) are given by

$$T_{\mathrm{f}}^{*} = \frac{T_{\mathrm{ad}}\bar{c}_{\mathrm{p,f}}}{Q},$$

$$\epsilon = \frac{T_{\mathrm{ad}}R_{\mathrm{u}}}{E_{\mathrm{a}}},$$

and

$$B = \frac{Q\sigma + \bar{c}_{\mathrm{p,f}}(T_{\infty} - \bar{T}_{\mathrm{s}})}{L}, \tag{22}$$

where Q is the lower heating value of the fuel, σ is the stoichiometric fuel-to-oxidizer (including inert species) mass ratio, $\bar{T}_{\mathrm{s}}$ is the average droplet surface temperature, L is the latent heat of vaporization of the fuel, and $\bar{c}_{\mathrm{p,f}}$ is the specific heat capacity of the fuel evaluated at $\bar{T} = 0.5(T_{\mathrm{ad}} + \bar{T}_{\mathrm{s}})$. The property correlations from the code were used to evaluate the parameters in the above equations. The specific results and methods employed include: for n-heptane combustion in dry air $Q = 44922$ kJ/kg and $\sigma = 0.06623$, for all cases $\bar{T}_{\mathrm{s}} = 355$ K, the latent heat of vaporization is evaluated at $\bar{T}_{\mathrm{s}}$ which yields $L = 322.5$ kJ/kg and the adiabatic flame temperature (neglecting dissociation) is evaluated by assuming that the fuel is supplied at $\bar{T}_{\mathrm{s}}$ and the air is supplied at T_{∞}.

The numerical results in Fig. 13 appear to collapse onto a single curve. The figure also shows a correlation (solid line) of the form

$$\mathrm{Da}_{\mathrm{M,e}}\left(T_{\mathrm{f}}^{*}\epsilon\right)^{3}(1+B) = (-3.24\times10^{-3} + 0.312\,\mathrm{Re}_{\mathrm{M,e}})\,\mathrm{Re}_{\mathrm{M,e}}^{Z}, \tag{23}$$

where

$$Z = -0.140 - 9.44\times10^{-2}w - 0.100w^{2} + 3.21\times10^{-2}w^{3}$$

and $w = \log \mathrm{Re}_{\mathrm{M,e}}$. Both the numerical results and the correlation are for a fixed ambient composition (dry air). The correlation can be used to iteratively determine $U_{\infty,\mathrm{e}}$ given $\bar{T}_{\mathrm{s}}$, T_{∞}, and d. Using $\bar{T}_{\mathrm{s}} = 355$ K and a relative error of $(U_{\infty,\mathrm{e}}(\mathrm{num}) - U_{\infty,\mathrm{e}}(\mathrm{corr}))/U_{\infty,\mathrm{e}}(\mathrm{num})$, where num indicates the numerical result and corr indicates the result from the correlation, the maximum errors are +11.8% for $d = 1$ mm and $T_{\infty} = 300$ K and −19.6% for $d = 0.5$ mm and $T_{\infty} = 1400$ K. These errors assume a priori knowledge of $\bar{T}_{\mathrm{s}}$ to use in the calculations. If the boiling temperature is used as the surface temperature ($\bar{T}_{\mathrm{s}} = 371.6$ K), the values for T_{ad}, $\bar{c}_{\mathrm{p,f}}$, L, T_{f}^{*}, ϵ, and B change only slightly. The resulting maximum relative errors in $U_{\infty,\mathrm{e}}$ are +11.1% for $d = 1$ mm, and $T_{\infty} = 300$ K and −21.9% for $d = 0.5$ mm and $T_{\infty} = 1400$ K.

The correlation given by Eq. (23) predicts extinction velocities over the range $0.15 < \mathrm{Re}_{\mathrm{M,e}} < 200$ that are in good agreement with the numerical results for n-heptane droplets in air at atmospheric pressure. A discussion of the form of the correlation, which is based on the asymptotic results of Krishnamurthy et al. [25] and Wu et al. [26], and the method of fitting the correlation to the data is presented in Appendix A key assumption that is shared by the asymptotic results [25] and the current numerical model is a one-step overall reaction that is first order with respect to fuel and first order with respect to oxidizer. It should also be noted that the correlation presented above does not contain a correction for varying ambient oxygen concentration.

5. Conclusions

The extinction of n-heptane droplets due to forced convection was studied using a quasi-steady numerical model. A new multicomponent formulation, which is appropriate for use with the finite-volume method, was developed to accurately describe the mass diffusion. Combustion was modeled using finite-rate chemical kinetics and a one-step overall chemical reaction. The chemical kinetic parameters used in the present study gave numerical results for n-heptane that were in quantitative agreement with the limited available n-heptane data and in qualitative agreement with experimental results for a variety of fuels and over a wide range of ambient temperatures and droplet diameters.

The results of this study establish the following: (a) Extinction velocity varies linearly with droplet diameter only for very large droplets ($d > 2$ mm), which is the present state of knowledge. For smaller droplets, however, the extinction velocity dependence on the droplet diameter is nonlinear. (b) The nonlinear variation of extinction velocity with droplet diameter for smaller droplets is a result of the transition of the flow field from a convection-dominated to an evaporation (mass diffusion)-dominated region. (c) Buoyancy-induced flows may be important for convective droplet extinction experiments conducted with suspended droplets at low ambient temperatures. (d) The extinction velocity varies exponentially with the ambient temperature.

The predicted extinction conditions, which cover a wide range of droplet diameters and ambient temperatures, can be represented by a single correlation. A form of the Damköhler number at extinction was correlated with the Reynolds number through the use of the transfer number and appropriate dimensionless activation and adiabatic flame temperatures. The correlation was developed based on results available in the literature for large activation energy asymptotics [25,26]. The current numerical predictions were for a fixed ambient composition (dry air), and the correlation does not contain a correction for varying ambient oxygen concentration.

Acknowledgments

This research was partially funded by NASA EPSCoR under Grant NCC5-401 and ARO EPSCoR under Grant DAAD19-99-1-0116. Computational resources were provided by the Thermal/Fluids Computational Facility and the Research Computing Facility at the University of Nebraska—Lincoln.

Appendix A

In this Appendix, the asymptotic analyses of Krishnamurthy et al. [25] and Wu et al. [26] are used to develop a correlation for the extinction of an envelope flame surrounding a liquid fuel droplet under forced convection. The asymptotic analyses were originally presented for the extinction of the diffusion flame formed between an oxidizer stream and a vaporizing fuel particle toward which the stream is flowing. A discussion of the reduction of the asymptotic results to a form that can be correlated is given below. The composition of the ambient oxidizer (dry air) is assumed to be fixed. Finally, the method used to generate the correlation is presented.

A.1. Form of correlation

The subscripts ∞ and s are used to denote conditions in the oxidizer stream and at the fuel surface, respectively. Given the notation used in the present work, the asymptotic results (for axisymmetric flow) of Krishnamurthy et al. [25] and Wu et al. [26] for extinction in the diffusion-flame regime can be written in the form

$$\frac{A}{2(\mathrm{d}u_\infty/\mathrm{d}r)}\rho\frac{1}{W_\mathrm{f}}\exp\left[\frac{-E_\mathrm{a}}{R_\mathrm{u}T_\mathrm{ad}}\right] = \frac{(e/2)}{(T_\mathrm{f}^*\epsilon)^3}\left[\frac{(1+\sigma Y_{\mathrm{ox},\infty})F_\mathrm{F}}{(1+B)}\right]^2 G(c), \tag{A.1}$$

where A is the preexponential factor, $\mathrm{d}u_\infty/\mathrm{d}r$ is the stretch rate in the oxidizer stream, ρ is the density, W_f is the molecular weight of the fuel, E_a is the activation energy, R_u is the universal gas constant, T_ad is the adiabatic flame temperature, $T_\mathrm{f}^* = T_\mathrm{ad}\bar{c}_{\mathrm{p,f}}/Q$ is the dimensionless adiabatic flame temperature, Q is the lower heating value of the fuel, $\epsilon = T_\mathrm{ad}R_\mathrm{u}/E_\mathrm{a}$ is the ratio of the adiabatic flame temperature to the activation temperature, $Y_{\mathrm{ox},\infty}$ is the mass fraction of oxidizer (including inert species) in the oxidizer stream, σ is the stoichiometric fuel to oxidizer (including inert species) mass ratio, B is the transfer number, and F_F and $G(c)$ are functions that are defined below. The adiabatic flame temperature, as opposed to the actual flame temperature, was used in writing Eq. (A.1) as recommended by Krishnamurthy et al. [25]. Also, $\bar{c}_{\mathrm{p,f}}$, which is the specific heat capacity of the fuel evaluated at $\bar{T} = 0.5(T_\mathrm{ad} + \bar{T}_\mathrm{s})$, where $\bar{T}_\mathrm{s}$ is the (average) temperature at the fuel surface, has been used to calculate dimensionless temperatures. Noting that $Y_{\mathrm{ox},\infty} = 1$, and assuming that the oxidizer is consumed in the flame ($Y_{\mathrm{ox,s}} = 0$, see Fig. 6), the resulting transfer number is

$$B = \frac{Q\sigma + \bar{c}_{\mathrm{p,f}}(T_\infty - \bar{T}_\mathrm{s})}{L},$$

where L is the latent heat of vaporization of the fuel. In the results of Wu et al. [26], the approximation $\mathrm{d}u_\infty/\mathrm{d}r = 3U_\infty/d$ was used from the solution for potential flow over a sphere. This approximation states that the stretch rate is proportional to the characteristic flow time (U_∞/d). If $\mathrm{d}u_\infty/\mathrm{d}r \propto U_\infty/d$ is used, the left-hand side of Eq. (A.1) differs from $\mathrm{Da}_{\mathrm{M,e}}$ defined by Eq. (21) by only a multiplicative constant and the "mean" conditions (designated by a subscript M) that are used to evaluate the properties (density).

Based on the observations given above, Eq. (A.1) can be rearranged to form

$$\mathrm{Da}_{\mathrm{M,e}}\left(T_{\mathrm{f}}^{*}\epsilon\right)^{3} \propto \left[\frac{(1+\sigma Y_{\mathrm{ox},\infty})F_{\mathrm{F}}}{(1+B)}\right]^{2} G(c), \qquad \text{(A.2)}$$

where the subscript M indicates an as yet unspecified "mean" condition for evaluating properties. The function $G(c)$ in Eq. (A.2) is defined as

$$G(c) = c(1 - 2c - 1.04c^2 + 0.44c^3), \qquad \text{(A.3)}$$

where

$$c = \begin{cases} (\sigma Y_{\mathrm{ox},\infty} + \beta)/(1+\sigma Y_{\mathrm{ox},\infty}) \\ \quad \text{if } \sigma Y_{\mathrm{ox},\infty} + 2\beta < 1, \\ (1-\beta)/(1+\sigma Y_{\mathrm{ox},\infty}) \\ \quad \text{if } \sigma Y_{\mathrm{ox},\infty} + 2\beta > 1, \end{cases} \qquad \text{(A.4)}$$

and the parameter β is given by

$$\beta = \frac{L + \bar{c}_{\mathrm{p,f}}(T_\infty - \bar{T}_{\mathrm{s}})}{Q}.$$

For all of the numerical results, $\sigma Y_{\mathrm{ox},\infty} + 2\beta < 1$, and the maximum value of $\sigma Y_{\mathrm{ox},\infty} + 2\beta$ is 0.3 at $T_\infty = 1400$ K. Krishnamurthy et al. [25] state that the parenthetic term in Eq. (A.3) is approximately one when $\sigma Y_{\mathrm{ox},\infty} + 2\beta \ll 1$. Adopting this approximation, the function $G(c)$ can be written as

$$G(c) \approx c = \frac{L}{Q}\frac{(1+B)}{(1+\sigma Y_{\mathrm{ox},\infty})}.$$

The current numerical results are for constant $Y_{\mathrm{ox},\infty} = 1$, σ, L, and Q. Substituting the approximation for $G(c)$ into Eq. (A.2), dropping the constant multiplicative terms, and rearranging yield

$$\mathrm{Da}_{\mathrm{M,e}}\left(T_{\mathrm{f}}^{*}\epsilon\right)^{3}(1+B) \propto F_{\mathrm{F}}^{2}. \qquad \text{(A.5)}$$

The function F_{F} in Eq. (A.5) is determined from the solution for the flow in the stagnation-point boundary layer. It is given by

$$F_{\mathrm{F}} = f_{\mathrm{s}} \exp\left[-\int_0^{\eta_{\mathrm{f}}} f\,\mathrm{d}\eta\right], \qquad \text{(A.6)}$$

where f is the dimensionless stream function, η is the transformed coordinate [25,26], and the subscript f indicates the location of the flame. The flow surrounding a droplet at extinction should be characterized by the Reynolds number. Thus, considering F_{F} as a function of $\mathrm{Re}_{\mathrm{M,e}}$ is a reasonable assumption, given an appropriate "mean" condition for evaluating the properties in the Reynolds number. The correctness of this assumption is verified in Fig. 13, which shows that the numerical results collapse onto a single curve. Several different methods of defining the mean conditions were attempted before adopting the definition used in the present work. Mean temperatures (T_{M}) of $0.5(T_\infty + \bar{T}_{\mathrm{s}})$, $0.5(T_{\mathrm{ad}} + T_\infty)$, and $0.5(T_{\mathrm{ad}} + \bar{T}_{\mathrm{s}})$ as well as combinations of Spalding's 1/3 rule [28] were used. Mean compositions that were explored include all fuel, all oxidizer, and the arithmetic mean of the droplet surface and the freestream composition. The use of Renksizbulut and Yuen's [54] definition for mean Reynolds number was also investigated. The definition for the mean condition that is adopted in the present work resulted in the best correlation of the numerical data.

A.2. Method of correlation

The remaining problem consists of defining the function F_{F}^2 in Eq. (A.5) in terms of $\mathrm{Re}_{\mathrm{M,e}}$. Using equation (A.6) for F_{F}, F_{F}^2 can be written as

$$F_{\mathrm{F}}^2 = \Psi\Omega,$$

where $\Psi = f_{\mathrm{s}}^2$ and

$$\Omega = \exp\left[-2\int_0^{\eta_{\mathrm{f}}} f\,\mathrm{d}\eta\right]. \qquad \text{(A.7)}$$

The function Ψ is simply the square of the dimensionless stream function evaluated at the fuel surface (f_{s}) which is related to the normal mass flux at the fuel surface [25]. The effect of convection on the normal mass flux at the fuel surface should be similar to the effect convection has on the evaporation constant. This effect is either a square-root dependence on Reynolds number [21] or a linear dependence on Reynolds number. The function $\Psi = f_{\mathrm{s}}^2$ should therefore have one of the following two forms:

$$\Psi = \begin{cases} \sum_{i=0}^{n} a_i\,\mathrm{Re}_{\mathrm{M,e}}^{i} & \text{for } n = 1, 2, \\ \sum_{i=0}^{n} a_i\,\mathrm{Re}_{\mathrm{M,e}}^{i/2} & \text{for } n = 2, 3, 4. \end{cases} \qquad \text{(A.8)}$$

Here the a_i's are the polynomial coefficients and n is the order of the polynomial. While some insight into the variation of the function Ψ with $\mathrm{Re}_{\mathrm{M,e}}$ is possible, the same cannot be said for the function Ω. Equation (A.7) indicates that Ω is a complicated function of the flow solution. The function Ω was assumed to be one of four forms in the curve-fitting process, either $\Omega =$

$\mathrm{Re}_{\mathrm{M,e}}^{\gamma}$ or $\Omega = \exp(\gamma)$, with the exponent γ taking on one of two forms:

$$\gamma = \begin{cases} \sum_{j=0}^{m} b_j \log^j \mathrm{Re}_{\mathrm{M,e}}, \\ \sum_{j=0}^{m} b_j \mathrm{Re}_{\mathrm{M,e}}^{j}. \end{cases} \tag{A.9}$$

Here the b_j's are the polynomial coefficients and m is the order of the polynomial.

The eight combinations of the functions Ψ and Ω described above were used to determine the best fit for the numerical data. For each combination, n was varied as shown in Eq. (A.8) and m was varied from 1 to 5. An iterative least-squares curve fit was performed using the following procedure: starting with an initial guess for the b_j's, (1) perform the curve fit to find the a_i's while holding the b_j's constant, (2) perform the curve fit to find the b_j's while holding the a_i's constant, and (3) repeat steps (1) and (2) until the a_i's and b_j's converge. The combination of functions (Ψ and Ω) and polynomial orders (n and m) that gave the lowest sum of the squared errors was the final correlation adopted in the present work. This correlation is given by Eq. (23).

References

[1] V. Nayagam, J.B. Haggard Jr., F.A. Williams, Dynamics of droplet extinction in slow convective flows, in: Fifth International Microgravity Combustion Workshop, NASA/CP-1999-208917, NASA Lewis Research Center, Cleveland, OH, 1999, pp. 461–464.

[2] R.L. Peskin, C.E. Polymeropoulos, P.S. Yeh, AIAA J. 5 (1967) 2173–2178.

[3] B.H. Chao, C.K. Law, J.S. Tíen, Proc. Combust. Inst. 23 (1990) 523–531.

[4] D.L. Dietrich, J.B. Haggard Jr., F.L. Dryer, V. Nayagam, B.D. Shaw, F.A. Williams, Proc. Combust. Inst. 26 (1996) 1201–1207.

[5] V. Nayagam, J.B. Haggard Jr., R.O. Colantonio, A.J. Marchese, F.L. Dryer, B.L. Zhang, F.A. Williams, AIAA J. 36 (1998) 1369–1378.

[6] D.B. Spalding, Fuel 32 (1953) 169–185.

[7] M. Goldsmith, Jet Propulsion 26 (1956) 172–178.

[8] G.A. Agoston, H. Wise, W.A. Rosser, Proc. Combust. Inst. 6 (1957) 708–717.

[9] H. Sami, M. Ogasawara, Bull. JSME 13 (57) (1970) 395–404.

[10] S.R. Gollahalli, T.A. Brzustowski, Proc. Combust. Inst. 14 (1973) 1333–1344.

[11] S.R. Gollahalli, T.A. Brzustowski, Proc. Combust. Inst. 15 (1975) 409–417.

[12] J.P. Gore, W. Meng, J. Jang, Combust. Flame 82 (1990) 126–141.

[13] V.R. Kuznetsov, V.A. Sabel'nikov, Turbulence and Combustion, Hemisphere, 1990, pp. 288–291.

[14] C.K. Law, G.M. Faeth, Prog. Energy Combust. Sci. 20 (1994) 65–113.

[15] H.A. Dwyer, B.R. Sanders, Proc. Combust. Inst. 21 (1986) 633–639.

[16] H.A. Dwyer, B.R. Sanders, Proc. Combust. Inst. 22 (1988) 1923–1929.

[17] K. Madooglu, A.R. Karagozian, Combust. Flame 94 (1993) 321–329.

[18] L. Weei Huang, C. Hsun Chen, Numer. Heat Transfer A 27 (1995) 53–71.

[19] T.L. Jiang, W.S. Chen, M.J. Tsai, H.H. Chiu, Combust. Flame 103 (1995) 221–238.

[20] J.C. Lee, A.G. Tomboulides, S.A. Orszag, R.A. Yetter, F.L. Dryer, Proc. Combust. Inst. 26 (1996) 3059–3065.

[21] S. Okajima, S. Kumagai, Proc. Combust. Inst. 19 (1982) 1021–1027.

[22] I. Gökalp, C. Chauveau, J.R. Richard, M. Kramer, W. Leuckel, Proc. Combust. Inst. 22 (1988) 2027–2035.

[23] F.E. Fendell, J. Fluid Mech. 21 (1965) 281–303.

[24] A. Liñán, Acta Astronaut. 1 (1974) 1007–1039.

[25] L. Krishnamurthy, F.A. Williams, K. Seshadri, Combust. Flame 26 (1976) 363–377.

[26] X. Wu, C.K. Law, A.C. Fernandez-Pello, Combust. Flame 44 (1982) 113–124.

[27] D.N. Pope, Numerical Simulation of Convective Fuel Droplet Vaporization and Combustion in a Low Pressure Zero-Gravity Environment, Ph.D. thesis, University of Nebraska—Lincoln, Lincoln, 2001.

[28] C.K. Law, Prog. Energy Combust. Sci. 8 (1982) 171–201.

[29] S.V. Patankar, Numerical Heat Transfer and Fluid Flow, Hemisphere, 1980.

[30] R.B. Bird, W.E. Stewart, E.N. Lightfoot, Transport Phenomena, Wiley, New York, 1960.

[31] T.P. Coffee, J.M. Heimerl, Combust. Flame 43 (1981) 273–289.

[32] R.C. Reid, J.M. Prausnitz, B.E. Poling, The Properties of Gases and Liquids, McGraw–Hill, New York, 1987.

[33] T.H. Chung, M. Ajlan, L.L. Lee, K.E. Starling, Ind. Eng. Chem. Res. 27 (1988) 671–679.

[34] C.R. Wilke, J. Chem. Phys. 18 (1950) 517–519.

[35] B.J. McBride, G. Sanford, M.A. Reno, Coefficients for Calculating Thermodynamic and Transport Properties of Individual Species, NASA Tech. Memorandum 4513, 1993.

[36] J.O. Hirschfelder, C.F. Curtiss, R.B. Bird, Molecular Theory of Gases and Liquids, Wiley, New York, 1954.

[37] G. Dixon-Lewis, Proc. R. Soc. London Ser. A 307 (1968) 111–135.

[38] J.D. Ramshaw, J. Non-Equilib. Thermodyn. 18 (1993) 121–134.

[39] R.J. Haywood, Variable-Property, Blowing and Transient Effects in Convective Droplet Evaporation with Internal Circulation, M.A.Sc. thesis, University of Waterloo, Ontario, 1986.

[40] R. Seiser, L. Truett, D. Trees, K. Seshadri, Proc. Combust. Inst. 27 (1998) 649–657.

[41] J.P. VanDoormaal, G.D. Raithby, Numer. Heat Transfer 7 (1984) 147–163.

[42] M. Vinokur, J. Comput. Phys. 50 (1983) 215–234.

[43] K.A. Cliffe, D.A. Lever, A Finite-Element Study of Isothermal, Laminar Flow Past a Sphere at Low and Intermediate Reynolds Numbers, Tech. Rep. AERE-R10868, Theoretical Physics Division, AERE, Harwell, Oxfordshire, August 1983.

[44] B. Fornberg, J. Fluid Mech. 190 (1988) 471–489.

[45] A.E. Hamielec, T.W. Hoffman, L.L. Ross, AIChE J. 13 (1967) 212–219.
[46] N.N. Sayegh, W.H. Gauvin, AIChE J. 25 (1979) 522–534.
[47] S.R.R. Dennis, J.D.A. Walker, J. Fluid Mech. 48 (1971) 771–789.
[48] R. Clift, J.R. Grace, M.E. Weber, Bubbles, Drops, and Particles, Academic Press, New York, 1978.
[49] S. Taneda, J. Phys. Soc. Japan 11 (1956) 1104–1108.
[50] K.A. Cliffe, D.A. Lever, Isothermal Flow Past a Blowing Sphere, Tech. Rep. TP.1042, Theoretical Physics Division, AERE, Harwell, Oxfordshire, May 1984.
[51] B.P. LeClair, A.E. Hamielec, H.R. Pruppacher, W.D. Hall, J. Atmos. Sci. 29 (1972) 728–740.
[52] C.H. Chiang, M.S. Raju, W.A. Sirignano, Int. J. Heat Mass Transfer 35 (1992) 1307–1324.
[53] M. Renksizbulut, M.C. Yuen, ASME J. Heat Transfer 105 (1983) 389–397.
[54] M. Renksizbulut, M.C. Yuen, ASME J. Heat Transfer 105 (1983) 384–388.
[55] C. Chauveau, X. Chesneau, I. Gökalp, Burning characteristics of *n*-heptane droplets under different regimes, in: AIAA—31st Aerospace Sciences Meeting and Exhibit, AIAA 93-0824, Reno, NV, 1993.